

# Electrical Transport Properties of Vanadium-Doped $\text{Bi}_2\text{Te}_{2.4}\text{Se}_{0.6}$

Christian Riha, Birkan Düzel, Karl Graser, Olivio Chiatti,\* Evangelos Golias, Jaime Sánchez-Barriga, Oliver Rader, Oleg E. Tereshchenko, and Saskia F. Fischer\*

Vanadium-doped  $\text{Bi}_{2-x}\text{Te}_{2.4}\text{Se}_{0.6}$  single crystals, with  $x = 0.015$  and  $0.03$ , are grown by the Bridgman method. Bandstructure characterization by angle-resolved photoemission spectroscopy (ARPES) measurements shows gapless topological surface states for both vanadium concentrations. The Van-der-Pauw resistivity, the Hall charge carrier density, and the mobility in the temperature range from  $0.3$  to  $300$  K are strongly dependent on vanadium concentration, with carrier densities as low as  $1.5 \times 10^{16} \text{ cm}^{-3}$  and mobilities as high as  $570 \text{ cm}^2 \text{ V}^{-1} \text{ s}^{-1}$ . As expected for transport in gapless topological surface states, the resistivity, carrier density, and mobility are constant below  $10$  K. The magnetoresistance shows weak antilocalization for both vanadium concentrations in the same temperature range. The weak antilocalization is analyzed with the Hikami–Larkin–Nagaoka model, which yields phase-coherence lengths of up to  $250 \text{ nm}$  for  $x = 0.015$ .

## 1. Introduction

Topological insulators (TIs) have received a lot of interest in recent years due to their possible applications in spintronics and quantum computation. This interest derives from the topological surface states (TSSs) that allow the observation of a variety of quantum effects,<sup>[1,2]</sup> some of which require magnetic

doping of the TI.<sup>[3,4]</sup> Effects of magnetic impurities on the band structure of TIs is presently under debate.<sup>[5]</sup>

Due to its relatively high energy gap of  $0.3 \text{ eV}$  and its simple surface-state structure, a considerable amount of effort has been put into the investigation of  $\text{Bi}_2\text{Se}_3$ . However, the transport properties of the TSSs are often masked by the bulk contribution due to the presence of Se vacancies and the resulting  $n$ -type doping.<sup>[6–8]</sup> A similar effect occurs in  $\text{Bi}_2\text{Te}_3$  due to Bi–Te antisite defects.<sup>[9]</sup> Both TIs have the tetradymite structure which allows to form  $\text{Bi}_2\text{Te}_2\text{Se}$  with a quintuple layer unit of Te–Bi–Se–Bi–Te.<sup>[10]</sup> This ternary TI is reasonably insulating compared with  $\text{Bi}_2\text{Se}_3$  and  $\text{Bi}_2\text{Te}_3$  and yields a resistivity which exceeds  $1 \Omega \text{ cm}$ . In this material system, the strong bonding

suppresses both the Se vacancies and the Te–Bi antisite defects.<sup>[11]</sup> These desirable properties make  $\text{Bi}_2\text{Te}_2\text{Se}$  a promising candidate to investigate the TSSs. Among the  $\text{Bi}_2\text{Te}_{3-x}\text{Se}_x$  materials, the  $\text{Bi}_2\text{Te}_{2.4}\text{Se}_{0.6}$  alloy is known to have one of the widest bandgaps.<sup>[12]</sup> In  $\text{V}_x\text{Bi}_{2-x}\text{Se}_3$  materials with a vanadium concentration of  $x = 0.04$ , angle-resolved photoemission spectroscopy (ARPES) measurements at  $100 \text{ K}$  revealed the opening of a non-magnetic energy gap of  $\approx 180 \text{ meV}$  in the surface states.<sup>[4]</sup>

Magnetically doped ternary<sup>[13]</sup> and nonternary<sup>[4,14]</sup> TIs allow to observe the quantum anomalous Hall effect, which may enable the development of low-power-consumption electronics. Other investigations involve the systematic crossover between weak antilocalization (WAL) and weak localization with the change of magnetic impurity concentration.<sup>[3]</sup> However, to date, investigations of electrical transport in magnetically doped  $\text{Bi}_2\text{Te}_{2.4}\text{Se}_{0.6}$  are still lacking.

In this work,  $\text{V}_x\text{Bi}_{2-x}\text{Te}_{2.4}\text{Se}_{0.6}$  crystals with  $x = 0.015$  and  $x = 0.03$  are investigated with respect to the electrical resistivity, the charge carrier concentration, and the mobility. In addition, low-field magnetotransport characteristics of the longitudinal resistance are studied to investigate WAL.


## 2. Results

The results of the ARPES measurements at  $T = 300 \text{ K}$  are shown in **Figure 1**. The TSSs and the Dirac point are visible in all samples. The Dirac point for undoped  $\text{Bi}_2\text{Te}_{2.4}\text{Se}_{0.6}$  is located at  $E_D = 0.28 \text{ eV}$  binding energy.<sup>[10]</sup> For  $\text{V}_x\text{Bi}_{2-x}\text{Te}_{2.4}\text{Se}_{0.6}$ , it shifts to higher binding energies:  $E_D = 0.33 \text{ eV}$  for  $x = 0.015$  and

Dr. C. Riha, B. Düzel, K. Graser, Dr. O. Chiatti, Prof. S. F. Fischer  
Novel Materials Group  
Humboldt-Universität zu Berlin  
10099 Berlin, Germany  
E-mail: [chiatti@physik.hu-berlin.de](mailto:chiatti@physik.hu-berlin.de); [sfischer@physik.hu-berlin.de](mailto:sfischer@physik.hu-berlin.de)

Dr. E. Golias, Dr. J. Sánchez-Barriga, Prof. O. Rader  
BESSY II  
Helmholtz-Zentrum-Berlin für Materialien und Energie  
12489 Berlin, Germany

Prof. O. E. Tereshchenko  
Physics Department  
Novosibirsk State University  
630090 Novosibirsk, Russia

 The ORCID identification number(s) for the author(s) of this article can be found under <https://doi.org/10.1002/pssb.202000088>.

© 2020 The Authors. Published by WILEY-VCH Verlag GmbH & Co. KGaA, Weinheim. This is an open access article under the terms of the Creative Commons Attribution License, which permits use, distribution and reproduction in any medium, provided the original work is properly cited.

Correction added on 27 November 2020, after first online publication.

DOI: [10.1002/pssb.202000088](https://doi.org/10.1002/pssb.202000088)

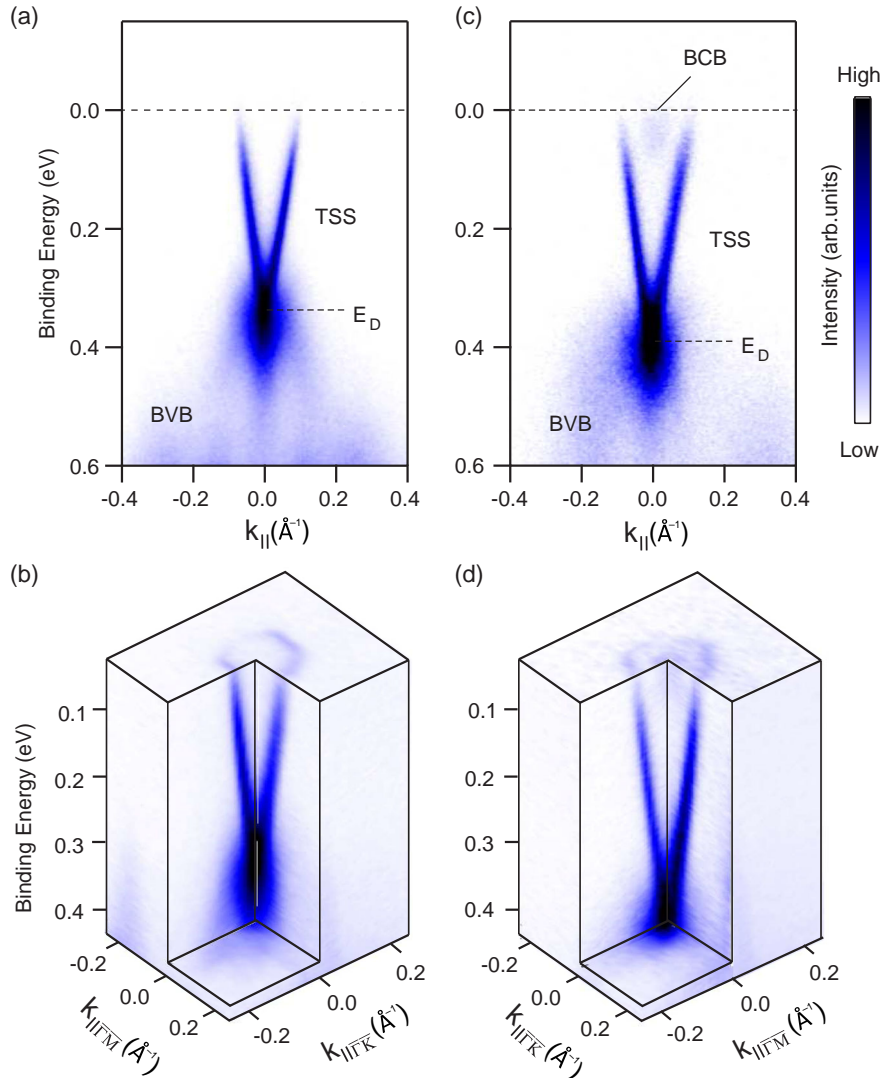


**Figure 1.** a,c) High-resolution ARPES dispersions and b,d) full photoemission mapping of the TSS of  $V_x\text{Bi}_{2-x}\text{Te}_{2.4}\text{Se}_{0.6}$  with (a,b)  $x=0.015$  and (c,d)  $x=0.03$ . In (a,c), bulk conduction band and bulk valence band states are denoted as BCB and BVB, respectively. The shift in the energy position of the Dirac point  $E_D$  with increasing V content is emphasized by horizontal dashed lines. The spectra were taken at  $T=300$  K using a photon energy of  $h\nu=66$  eV.

$E_D=0.38$  eV for  $x=0.03$ . The Fermi energy  $E_F$  appears to be located inside the bandgap for  $x=0.015$ . In the crystal with  $x=0.03$ , it appears to be close to the bulk conduction band. The Fermi wavevectors for the TSSs are  $k_{F,\text{TSS}}=0.084 \text{ \AA}^{-1}$  and  $k_{F,\text{TSS}}=0.10 \text{ \AA}^{-1}$  for  $x=0.015$  and  $x=0.030$ , respectively. This yields a charge carrier density in the TSSs of  $n_{\text{TSS}}=5.6 \times 10^{12} \text{ cm}^{-2}$  and  $n_{\text{TSS}}=8.0 \times 10^{12} \text{ cm}^{-2}$  for  $x=0.015$  and  $x=0.030$ , respectively.

The V-doped  $\text{Bi}_2\text{Te}_{2.4}\text{Se}_{0.6}$  single crystals are electrically characterized by performing Hall and Van-der-Pauw measurements in the temperature range of 0.3 to 300 K. The  $I$ - $V$  curves show ohmic characteristics in this temperature range.

The temperature-dependent sample resistivity  $\rho$  is shown in **Figure 2a**. The resistivity for  $x=0.015$  is approximately one order of magnitude higher than for  $x=0.03$ . All samples show a semiconducting-like temperature dependence of  $\rho$  above

$T=40$  K. However, below  $T=10$  K, we observe a nearly constant resistivity, which indicates the influence of the TSSs.

From Hall measurements, we observe  $n$ -type behavior. Under the assumption of one-band conductivity, the charge carrier density  $n$  is derived and shown in **Figure 2b**. At 300 K,  $n$  increases with increasing vanadium concentration  $x$ . In the temperature range between 10 K and 150 K, a strong temperature dependence of  $n$  is observed.  $n$  is approximately constant below  $T=10$  K. A minimum of  $n=1.5 \times 10^{16} \text{ cm}^{-3}$  for  $x=0.015$  is found at  $T=40$  K. The activation energy is determined from the slope of the Arrhenius equation  $\ln(n)=\ln(n^*)-(E_A/k_B) \cdot (1/T)$ , with the Boltzmann constant  $k_B$  and the high-temperature limit of the carrier density  $n^*$ . The fits are shown in **Figure 3**. The sample with  $x=0.03$  yields  $E_A=6.9$  meV. The sample with  $x=0.015$  yields  $E_A=24.9$  meV, supporting the observation by photoemission spectroscopy that  $E_F$  is located inside the bulk bandgap.

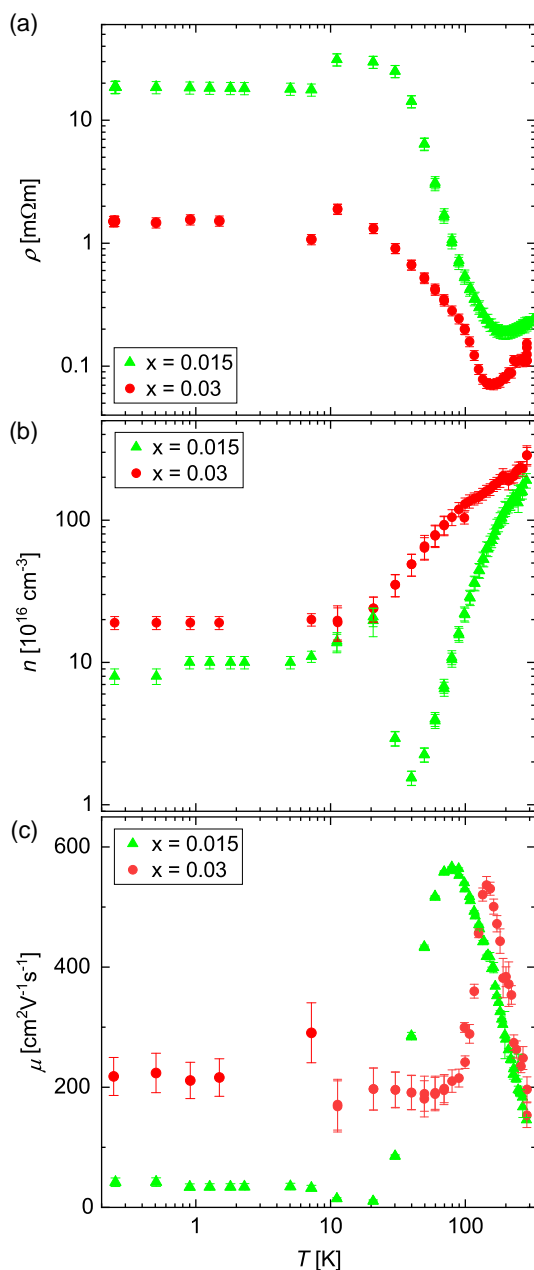


**Figure 2.** a) Temperature-dependent resistivity obtained from Van-der-Pauw measurements of  $V_x\text{Bi}_{2-x}\text{Te}_{2.4}\text{Se}_{0.6}$  crystals with  $x = 0.015$  and  $x = 0.03$ . From temperature-dependent Hall measurements, b) the charge carrier density  $n$  and c) the mobility  $\mu$  is obtained.

Under the assumption of one-band conductivity, the electron mobility  $\mu = 1/\rho en$  is calculated from the resistivity  $\rho$  and the carrier concentration  $n$ , and is shown in Figure 2c. Above  $T = 200$  K, the mobility  $\mu$  has the same values for all samples within the measurement uncertainty. Note that the Debye temperature of  $\text{Bi}_2\text{Te}_{2-x}\text{Se}_x$  is  $\Theta_D = 155$  K.<sup>[15]</sup> Below  $\Theta_D$  maxima of  $\mu$  are found:  $\mu_{\text{max}} = 570\text{ cm}^2\text{V}^{-1}\text{s}^{-1}$  at  $T = 80$  K for  $x = 0.015$  and  $\mu_{\text{max}} = 530\text{ cm}^2\text{V}^{-1}\text{s}^{-1}$  at  $T = 150$  K for  $x = 0.03$ . Below  $T = 20$  K, the mobility is constant for  $x = 0.015$  and  $x = 0.03$  at  $\mu_{0\text{K}} = 40\text{ cm}^2\text{V}^{-1}\text{s}^{-1}$  and  $\mu_{0\text{K}} = 220\text{ cm}^2\text{V}^{-1}\text{s}^{-1}$ , respectively.

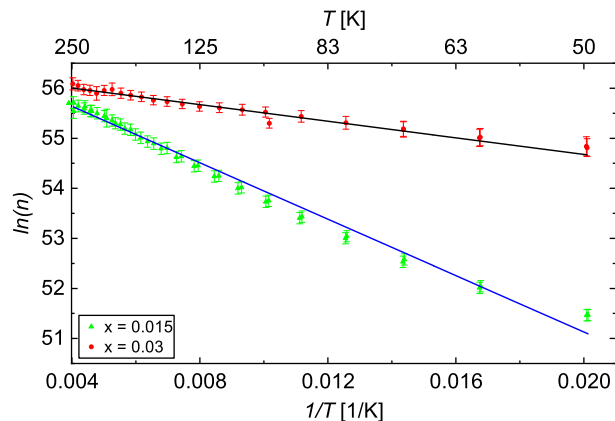


**Figure 3.** Arrhenius plot for  $V_x\text{Bi}_{2-x}\text{Te}_{2.4}\text{Se}_{0.6}$  crystals with  $x = 0.015$  and  $x = 0.03$ . The solid lines are fits to the Arrhenius equation (see text). The slopes yield  $E_A = 24.9$  meV and  $E_A = 6.9$  meV for  $x = 0.015$  and  $x = 0.03$ , respectively. The intercepts yield  $n^* = 4.5 \times 10^{18}\text{ cm}^{-3}$  and  $n^* = 2.9 \times 10^{18}\text{ cm}^{-3}$  for  $x = 0.015$  and  $x = 0.03$ , respectively.

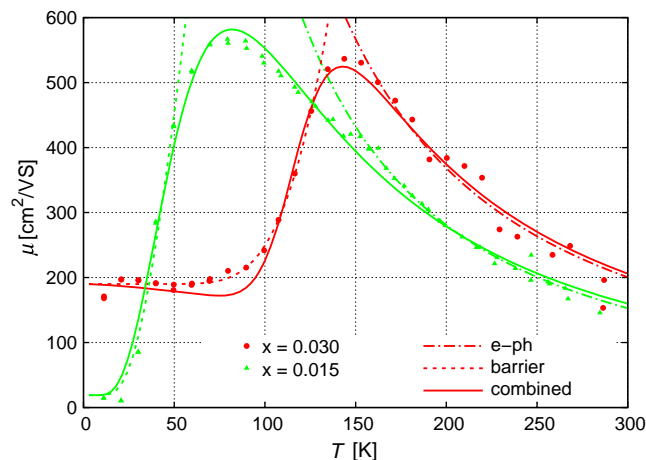


**Figure 4.** Fits of the mobility as a function of temperature for  $V_x\text{Bi}_{2-x}\text{Te}_{2.4}\text{Se}_{0.6}$  crystals with  $x = 0.015$  and  $x = 0.03$ . The dash-dotted lines are fits to electron-phonon (deformation potential) scattering, with a  $T^{-3/2}$  dependence. The dashed lines are fits to thermal activation over a barrier and with a constant background mobility, with an exponential temperature dependence. These fits yield a barrier height of  $\phi_B = 12$  meV and  $\phi_B = 68$  meV for  $x = 0.015$  and  $x = 0.03$ , respectively. The solid lines are the combination of both processes following the Matthiessen rule.

The Debye temperature  $\Theta_D$  separates the temperature dependence in two regimes (see Figure 4). In the high-temperature range, electron-phonon scattering dominates the mobility (dash-dotted lines in Figure 4). In the low-temperature range, the temperature dependence is consistent with an activation over a barrier, in addition to a constant background mobility (dashed lines in Figure 4). However, in the presence of multiple parallel conducting layers or bands, like the bulk states and the TSSs in this instance, a one-band analysis of the transport data can yield counter-intuitive results.<sup>[6]</sup> The measurement results are summarized in Table 1.

**Table 1.** Overview of the measurement results for the samples  $V_x\text{Bi}_{2-x}\text{Te}_{2.4}\text{Se}_{0.6}$  in this work: the thickness  $t$ ; the binding energy  $E_D$  of the Dirac point, the Fermi wavevector for the TSS  $k_{F,\text{TSS}}$ , and the corresponding charge carrier densities  $n_{\text{TSS}}$  from the ARPES measurements; charge carrier density  $n_{268\text{K}}$  at  $T = 268\text{ K}$  and its constant value at low temperatures  $n_{0\text{K}}$  from Hall measurements, the activation energy  $E_A$ ; the mobility  $\mu$  at  $T = 268\text{ K}$ , its maximum  $\mu_{\text{max}}$  and its saturation value for low temperatures  $\mu_{0\text{K}}$ , the temperature of the maximum mobility  $T_{\mu,\text{max}}$ ; the maximum of the phase-coherence length  $l_{\varphi,\text{max}}$  from the HLN fits, the highest temperature  $T_{\varphi,\text{max}}$  above which the WAL in the magnetoresistance is not observed; the highest temperature  $T^*$  above which the hysteresis in the magnetoresistance is not observed. See text for details.

$x$	0.015	0.03
$t$ [ $\mu\text{m}$ ]	170	650
$E_D$ [eV]	0.33	0.38
$k_{F,\text{TSS}}$ [ $\text{\AA}^{-1}$ ]	0.084	0.10
$n_{\text{TSS}}$ [ $10^{12}\text{ cm}^{-2}$ ]	5.6	8.0
$n_{268\text{K}}$ [ $10^{18}\text{ cm}^{-3}$ ]	1.6	2.3
$n_{0\text{K}}$ [ $10^{16}\text{ cm}^{-3}$ ]	8	19
$E_A$ [meV]	24.9	6.9
$\mu_{268\text{K}}$ [ $\text{cm}^2\text{ V}^{-1}\text{ s}^{-1}$ ]	190	250
$\mu_{\text{max}}$ [ $\text{cm}^2\text{ V}^{-1}\text{ s}^{-1}$ ]	570	530
$\mu_{0\text{K}}$ [ $\text{cm}^2\text{ V}^{-1}\text{ s}^{-1}$ ]	40	220
$T_{\mu,\text{max}}$ [K]	70	145
$l_{\varphi,\text{max}}$ [nm]	250	180
$T_{\varphi,\text{max}}$ [K]	$\approx 10$	$\approx 1$
$T^*$ [K]	2.3	0.9

The magnetoresistance is measured by applying a magnetic field perpendicular to the sample surface in the temperature range from  $T = 0.3\text{ K}$  to  $T = 10\text{ K}$ . The measurement data are shown for each sample in **Figure 5**. All samples show a dip in the resistance at zero field, which is consistent with WAL.<sup>[1]</sup> For higher fields, the magnetoresistance is approximately linear, as a result of the competition between the WAL cusp and the semiclassical  $B^2$ -dependence.<sup>[16]</sup>

At low temperatures, a sweeprate-dependent hysteresis in the magnetoresistance is observed in all samples. In **Figure 6a**, the time-dependent resistivity of the sample is depicted after sweeping the magnetic field from  $B = 0\text{ T}$  to  $B = 0.6\text{ T}$  with a sweeprate of  $\text{d}B/\text{d}T = 0.5\text{ T min}^{-1}$ . **Figure 6b** shows the reverse sweep. A ferromagnetic-like hysteresis is excluded because of this time-dependence. The hysteresis is more distinct at higher sweeprates of the magnetic field and vanishes at higher temperatures. For  $x = 0.015$  the temperature above which the hysteresis is not visible is  $T^* = 2.3\text{ K}$ , much higher than for  $x = 0.03$  (see **Table 1**).

To evaluate the negative magnetoresistance, the data taken at the smallest sweeprate are fitted with the Hikami–Larkin–Nagaoka (HLN) equation<sup>[17]</sup>

$$\begin{aligned} \Delta\sigma &= \sigma(B) - \sigma(0) \\ &= \alpha \frac{e^2}{2\pi^2\hbar} \left[ \ln\left(\frac{B_\varphi}{B}\right) - \Psi\left(\frac{1}{2} + \frac{B_\varphi}{B}\right) \right] \end{aligned} \quad (1)$$

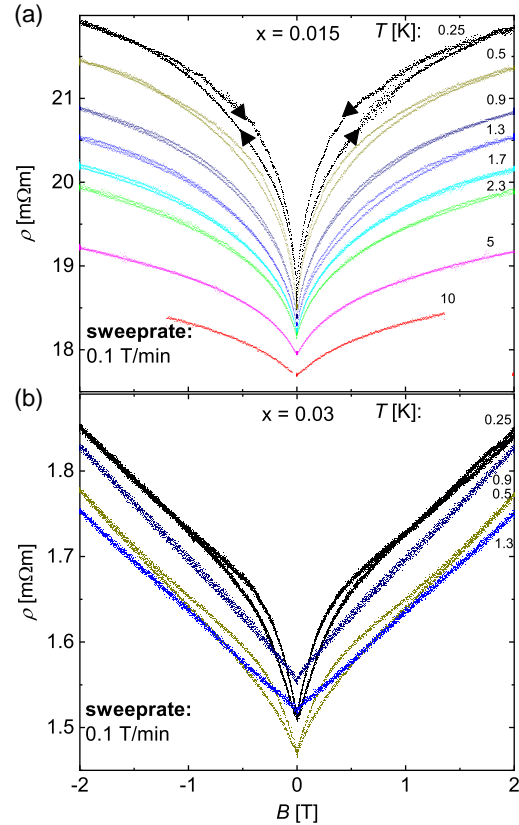


**Figure 5.** Measurement of the longitudinal magnetoresistivity at low magnetic fields of  $V_x\text{Bi}_{2-x}\text{Te}_{2.4}\text{Se}_{0.6}$  crystals with a)  $x = 0.015$  and b)  $x = 0.03$ . Arrows in (a) indicate whether the magnetic field is increasing or decreasing.

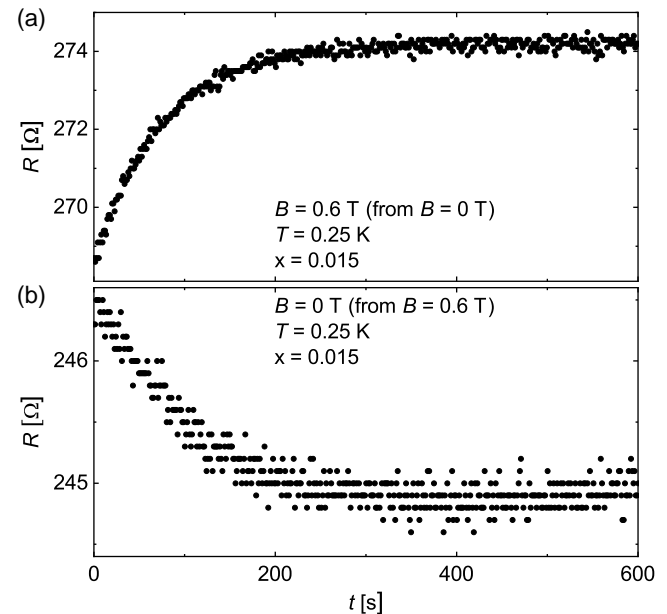


**Figure 6.** The change in the longitudinal resistance for the sample  $x = 0.015$  is shown at  $T = 0.3\text{ K}$  when the magnetic field is swept a) from  $B = 0$  to  $B = 0.6\text{ T}$  and b) from  $B = 0.6\text{ T}$  to  $B = 0$  with a rate of  $\text{d}B/\text{d}T = 0.5\text{ T min}^{-1}$ .

with the characteristic magnetic field  $B_\phi = \hbar/4el_\phi^2$ , expressed in terms of the phase-coherence length  $l_\phi$ , and the prefactor  $\alpha$ , which is expected to be  $-1$  for weak localization and  $+1/2$  for WAL<sup>[17]</sup> in 2D electron systems. The magnetoconductivity, after subtracting the background, and the applied fits are shown for  $x = 0.015$  in Figure 7a and  $x = 0.03$  in Figure 7b, respectively. The hysteresis is considered by applying the fit to each arm of the hysteresis separately and taking the average value of the

fit parameters  $B_\phi$  and  $\alpha$ . The parameter  $l_\phi$  derived from the fits is shown in Figure 7c. It decreases with increasing temperature, as is expected due to increasing scattering and thermal averaging. The parameter  $\alpha$  exceeds values for 2D conductors due to the contribution of the bulk conductivity.

### 3. Discussion

The photoemission spectra show a shift in the binding energy of the Dirac point  $E_D$  with increasing vanadium concentration  $x$ . The Fermi energy increases relative to  $E_D$  with increasing  $x$ . This is consistent with the increase in the charge carrier density with  $x$  observed in the Hall measurements. Calculations of energy spectra<sup>[10]</sup> yield a shift of the Fermi energy of up to 50 meV, depending on the type of disorder. This gives a disorder-induced uncertainty in the Fermi energy, which is larger than the change in activation energy derived from our data. In this work, both samples are expected to have the same type and degree of disorder, so a disorder-induced shift in the Fermi energy is not anticipated.

The temperature-dependent resistivity  $\rho(T)$  shows deviations from a semiconducting-like behavior by saturating at a constant value at lower temperatures. This can be attributed to a metallic-like behavior of the TSSs, as supported by the photoemission spectra. Transport in the TSSs is also consistent by the constant charge carrier density  $n$  in the low-temperature regime below  $T = 10$  K. Above  $T = 40$  K,  $n$  is thermally activated from donor states, which yield a bulk-dominated transport.

Although the one-band analysis is limited, the temperature dependence of the mobility  $\mu(T)$  above the Debye temperature  $\Theta_D = 155$  K shows a semiconducting-like behavior, i.e., it is dominated by electron-phonon scattering. Below  $\Theta_D$ , the temperature dependence is consistent with thermal activation across a barrier, with a constant mobility background. One possible origin for such a barrier is the formation of grain-like areas due to different distributions of Se atoms in the lattice,<sup>[10]</sup> with local changes in the bandstructure and in particular of the energy gap at the  $\Gamma$ -point. The barrier height is affected by the V concentration, by partially filling trap states at the interfaces between areas with mismatched bandstructures.

WAL is observed for all the V-doped  $\text{Bi}_2\text{Te}_{2.4}\text{Se}_{0.6}$  crystals, as expected for transport dominated by the TSSs. This may indicate that the V-concentration does not affect strongly the spin-orbit coupling and in consequence the band inversion. The phase-coherence length  $l_\phi$  from the fits yields values typical for TIs.<sup>[6]</sup> However, the values for  $\alpha$  are orders of magnitude larger than expected in purely 2D systems. This indicates that the magnetoresistance cannot be easily evaluated under this assumption.

Although the general behavior of the vanadium-doped  $\text{Bi}_2\text{Te}_{2.4}\text{Se}_{0.6}$  crystals can be understood, the following observations remain to be clarified. The  $x = 0.015$  appears to be a special case, with respect to the increased activation energy  $E_A$ , the strongly suppressed (one-band) mobility, the minimum in the (one-band) charge carrier density at  $T = 40$  K, and the enhanced phase-coherence length  $l_\phi$ . Possible explanations may be found in mechanisms of compensation doping and hole density due to thermal activation into a second band near the M-point.<sup>[10]</sup>

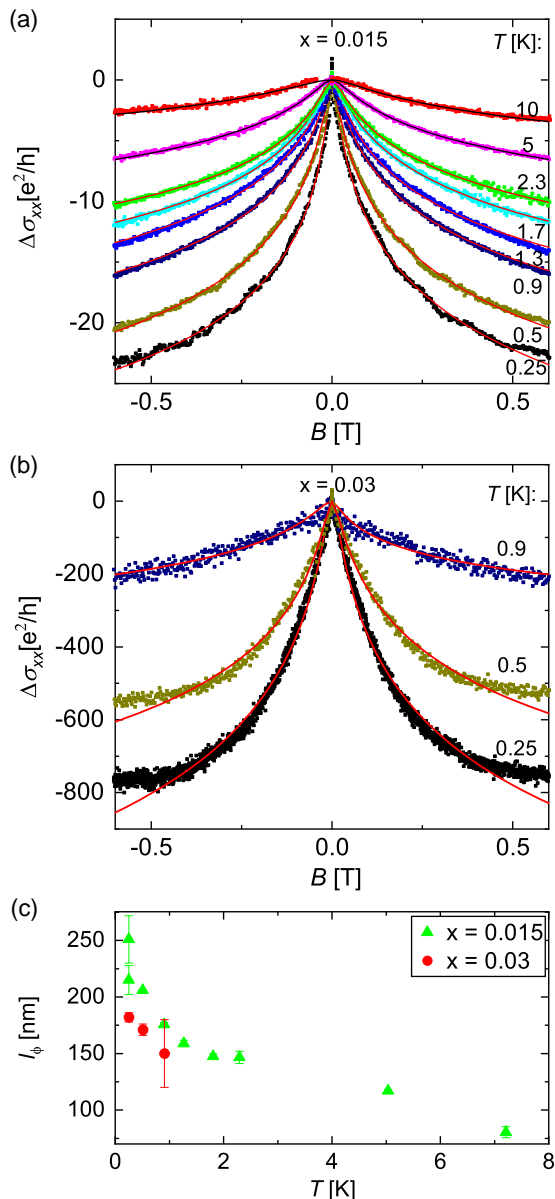


**Figure 7.** Low-field magnetoconductivity of  $\text{V}_x\text{Bi}_{2-x}\text{Te}_{2.4}\text{Se}_{0.6}$  bulk crystals at different temperatures, for a)  $x = 0.015$  and b)  $x = 0.03$ . The magnetoconductivity  $\Delta\sigma_{xx}$  is determined by subtracting a background (squares). The HLN equation is fitted to these data (solid lines). In c) the phase-coherence length  $l_\phi$  is extracted from the fits in (a) and (b) at different temperatures. The parameter  $\alpha$  varies between 7 and 20 for  $x = 0.015$ , and between 160 and 1200 for  $x = 0.03$ . These values are larger than for 2D conductors, because of parallel conduction from bulk states.



However, the increased  $l_\varphi$  and  $T_{\varphi,\max}$  indicate that inelastic scattering is reduced. The enhanced values of  $\alpha$  warrant further investigation.

Furthermore, the sweep-rate-dependent hysteresis in the magnetoresistance needs clarification. We propose as a possible origin a spin-dependent scattering for eddy currents in the TSSs. The higher surface conductivity due to the TSSs makes eddy currents more likely to be carried by the spin-momentum-locked TSSs. The dependence of the hysteresis on the sign of the time-derivative of the magnetic field is consistent with a scattering that depends on the direction of the eddy currents, which, for spin-momentum-locked states, could indicate a spin-dependent scattering.

## 4. Conclusion

We investigated  $V_x\text{Bi}_{2-x}\text{Te}_{2.4}\text{Se}_{0.6}$  single crystals. Photoemission spectra and resistivity measurements confirm the existence of the TSSs. The chemical potential is shifted with increasing vanadium concentration. For both vanadium concentrations, the photoemission spectra and the WAL in the magnetoresistance show that there is no gap at the Dirac point. For  $x = 0.015$ , we observed an increased phase-coherence length and maximum temperature for phase-coherent effects, which indicate suppressed inelastic scattering.

## 5. Experimental Section

$V_x\text{Bi}_{2-x}\text{Te}_{2.4}\text{Se}_{0.6}$  crystals with  $x = 0.015$  and  $x = 0.03$  were grown by the Bridgman method. The bandstructure of these crystals was characterized by angle-resolved photoemission spectroscopy (ARPES) at the ARPES1<sup>2</sup> station at the synchrotron radiation source BESSY II.

From these crystals, bulk samples with a surface of  $2\text{ mm} \times 5\text{ mm}$  and a thickness of  $t_{0.015} = (170 \pm 20)\text{ }\mu\text{m}$  and  $t_{0.03} = (650 \pm 60)\text{ }\mu\text{m}$  were cleaved and glued onto a  $\text{SiO}_2$  substrate with an oxide thickness of  $1\text{ }\mu\text{m}$ . Ohmic contacts were established by Ag paint and wedge bonding with Al wires.

The contact pattern allowed to perform Hall and Van-der-Pauw measurements,<sup>[18]</sup> as well as measurements of the longitudinal resistance. The temperature-dependent Van-der-Pauw and Hall measurements were performed in a Konti Kryostat IT using Keithley SourceMeter Units. The magnetoresistance measurements were performed in a Helium-3-System HelioxVL using a Signal Recovery 7265 Lock-in Amplifier.

## Acknowledgements

The authors gratefully acknowledge financial support by the priority programme “Topological Insulators: Materials—Fundamental Properties—Devices” of the German Research Foundation DFG SPP 1666. J. S.-B. gratefully acknowledges financial support from the “Impuls- und Vernetzungsfonds der Helmholtz-Gemeinschaft” under grant no. HRSF-0067 (Helmholtz–Russia Joint Research Group). Open access funding enabled and organized by Projekt DEAL.

## Conflict of Interest

The authors declare no conflict of interest.

## Keywords

photoemission, topological insulators, transport properties, weak antilocalization

Received: February 14, 2020

Revised: June 1, 2020

Published online: July 8, 2020

- [1] Y. Ando, *J. Phys. Soc. Jpn.* **2013**, *82*, 102001.
- [2] M. Z. Hasan, C. L. Kane, *Rev. Mod. Phys.* **2010**, *82*, 3045.
- [3] M. Liu, J. Zhang, C. Z. Chang, Z. Zhang, X. Feng, K. Li, K. He, L.-L. Wang, X. Chen, X. Dai, Z. Fang, Q.-K. Xue, X. Ma, Y. Wang, *Phys. Rev. Lett.* **2012**, *108*, 036805.
- [4] L. Zhang, D. Zhao, Y. Zang, Y. Yuan, G. Jiang, M. Liao, D. Zhang, K. He, X. Ma, Q. Xue, *APL Mater.* **2017**, *5*, 076106.
- [5] J. Sánchez-Barriga, A. Varykhalov, G. Springholz, H. Steiner, R. Kirchschrager, G. Bauer, O. Caha, E. Schierle, E. Weschke, A. Únal, S. Valencia, M. Dunst, J. Braun, H. Ebert, J. Minár, E. Golias, L. V. Yashina, A. Ney, V. Holý, O. Rader, *Nat. Commun.* **2016**, *7*, 10559.
- [6] O. Chiatti, C. Riha, D. Lawrenz, M. Busch, S. Dusari, J. Sánchez-Barriga, A. Mogilatenko, L. V. Yashina, S. Valencia, A. A. Únal, O. Rader, S. F. Fischer, *Sci. Rep.* **2016**, *6*, 27483.
- [7] M. Busch, O. Chiatti, S. Pezzini, S. Wiedmann, J. Sánchez-Barriga, O. Rader, L. V. Yashina, S. F. Fischer, *Sci. Rep.* **2018**, *8*, 485.
- [8] H. Cao, J. Tian, I. Miotkowski, T. Shen, J. Hu, S. Qiao, Y. P. Chen, *Phys. Rev. Lett.* **2012**, *108*, 216803.
- [9] D. Scanlon, P. King, R. P. Singh, A. De La Torre, S. M. Walker, G. Balakrishnan, F. Baumberger, C. Catlow, *Adv. Mater.* **2012**, *24*, 2154.
- [10] A. Shikin, I. Klimovskikh, S. Eremeev, A. Rybkina, M. Rusinova, A. Rybkin, E. Zhizhin, J. Sánchez-Barriga, A. Varykhalov, I. Rusinova, E. V. Chulkov, K. A. Kokh, V. A. Golyashov, V. Kamyshlov, O. E. Tereshchenko, *Phys. Rev. B* **2014**, *89*, 125416.
- [11] Z. Ren, A. Taskin, S. Sasaki, K. Segawa, Y. Ando, *Phys. Rev. B* **2010**, *82*, 241306.
- [12] I. Austin, A. Sheard, *Int. J. Electron.* **1957**, *3*, 236.
- [13] C. Z. Chang, J. Zhang, X. Feng, J. Shen, Z. Zhang, M. Guo, K. Li, Y. Ou, P. Wei, L. L. Wang, Z.-Q. Ji, Y. Feng, S. Ji, X. Chen, J. Jia, X. Dai, Z. Fang, S.-C. Zhang, K. He, Y. Wang, L. Lu, X.-C. Ma, Q.-K. Xue, *Science* **2013**, *340*, 167.
- [14] C. Z. Chang, W. Zhao, D. Y. Kim, H. Zhang, B. A. Assaf, D. Heiman, S. C. Zhang, C. Liu, M. H. Chan, J. S. Moodera, *Nat. Mater.* **2015**, *14*, 473.
- [15] G. Zheng, X. Su, T. Liang, Q. Lu, Y. Yan, C. Uher, X. Tang, *J. Mater. Chem. A* **2015**, *3*, 6603.
- [16] B. A. Assaf, T. Cardinal, P. Wei, F. Katmis, J. S. Moodera, D. Heiman, *Appl. Phys. Lett.* **2013**, *102*, 012102.
- [17] S. Hikami, A. I. Larkin, Y. Nagaoka, *Prog. Theor. Phys.* **1980**, *63*, 707.
- [18] L. J. Van der Pauw, *Philips Res. Rep.* **1958**, *13*, 1.